ADVANCED MATERIALS INTERFACES
www.advmatinterfaces.de

Optically Isotropic Liquid Crystal Mode Templated by Nanoporous Breath Figure Membrane

*Young-Chul Shin, Ji-Sub Park, Kyung-Il Joo, Hyun Gyu Kim, Ramesh Manda, Jun-Chan Choi, and Hak-Rin Kim**

In this study, a printing-based scalable method is proposed for the higher density of a liquid crystal (LC) nanodroplet structure suitable for the optically isotropic LC mode where the LC nanodomains are accurately templated by a nanoporous breath figure (BF) membrane. The highly porous BF polymeric template structure is reliably obtained by utilizing self-structured packing effects of the silica nanospheres achieved by doctor blade coating. A nanocomposite film with densely packed silica nanospheres encapsulated by the UV-crosslinked polymer matrix is made by controlling the blade coating velocity and blade gap conditions. This provides a higher LC fill-factor condition of the optically isotropic nanodroplet LC (OI-NDLC) mode with filling the LCs into the nanopores obtained after selective silica etching. The OI-NDLC structure templated by the nanoporous BF membrane made with the silica nanospheres of 300 nm can effectively resolve the scattering-induced optical loss and depolarization issues observable in the OI-NDLC mode prepared by conventional phase separation approaches due to the sufficiently reduced LC droplet size. The structure exhibits a much-improved light leakage level in the field-off optically isotropic state, a higher transmittance level as the field-induced Kerr operation, and resultant improved contrast ratio properties.

1. Introduction

Display form factors that can be technologically implemented recently became an increasingly important issue in mobile and automotive displays. Although the liquid crystal display (LCD) is improving its technological competitiveness with organic light-emitting diode (OLED) in almost every aspect of display technological issues such as visibility, resolution, panel power consumption, and color gamut,[1–5] the development of an innovative liquid crystal (LC) mode is still essentially required to enter novel display application fields such as curved, rollable, and flexible displays to compete with OLED's superior mechanical flexibility.[6] In contrast to OLED that is composed of thin organic solid layers, LCDs consist of fluidic LC molecules for transmittance level control by utilizing field-switchable birefringent effects. Thus, their electro-optical (EO) properties, such as transmittance in bright state, light leakage in dark state, contrast ratio (CR) levels, and LC texture uniformity, highly depend on the cell gap uniformity of LCDs, initial LC alignments, and LC geometries of the field-induced molecular reorientations. These LCD properties are highly sensitive to external stress conditions, such as local pressure and substrate bending because the LC orientations are distorted and the LCD cell gap is positionally varied under the externally deformed conditions.

As an LC mode that is more suitable for flexible displays, the polymer-dispersed liquid crystal (PDLC) has been widely studied in LCDs.[7–11] The PDLC structure is a valuable approach in achieving flexible display applications due to its various advantages, including simple fabrication without requiring alignment layers, high mechanical stability by the polymer matrix, wide and symmetric viewing angle properties, and large-scale applicability.[10,11] Contrary to conventional LCDs, the LC molecules in the PDLC structure are formed within randomly dispersed LC droplets encapsulated within the polymer matrix, which also have random distributions in their effective optic axis. Accordingly, several types of the phase separation process have been proposed to obtain this PDLC structure. These include polymerization-induced phase separation (PIPS), thermally induced phase separation, and solvent-induced phase separation.[8,9] Among these, PIPS is one of the most widely used methods for fabricating the PDLC structure because the PDLC morphologies, such as the LC droplet size and density, can be controlled by varying the phase separation conditions, such as the relative molecular mixing ratio between the LCs and the prepolymers,

Y.-C. Shin, R. Manda, J.-C. Choi, H.-R. Kim
School of Electronic and Electrical Engineering
Kyungpook National University
Daegu 41566, South Korea
E-mail: rineey@knu.ac.kr
Y.-C. Shin, J.-S. Park, H. G. Kim
LG Display Co. Ltd.
Paju, Gyeonggi-do 10845, South Korea
J.-S. Park, K.-I. Joo, H. G. Kim, H.-R. Kim
School of Electronics Engineering
Kyungpook National University
Daegu 41566, South Korea
K.-I. Joo
Spatial Optical Information Research Center
Korea Photonics Technology Institute
Gwangju 61007, South Korea

The ORCID identification number(s) for the author(s) of this article can be found under https://doi.org/10.1002/admi.202101919.

DOI: 10.1002/admi.202101919

and the UV reaction rate by UV intensity control.[9] However, to be applied to high-visibility display applications with a higher CR property, conventional PDLCs composed of microsized LC droplets, face difficulties in realizing an ideal black state under the electric field off condition and in achieving a higher light efficiency under the electric field on condition due to the depolarization effects of light scattering in both operation mode conditions.

These depolarization effects by the randomly distributed LC droplets can be effectively suppressed by reducing the LC droplet sizes to be smaller than visible wavelengths.[12–15] In the case of the nanodroplet LC (NDLC) structures, the optically isotropic (OI) LC mode can be obtained under the electric field off condition. This unusual OI phase of the NDLCs not only originates from the smaller droplets, but also from the random distribution of the birefringent axis at which the incident beam encounters a homogenous medium without scattering and simply passes through without depolarization effects and polarization changes. An OI-NDLC mode has many advantages for flexible LCD applications, such as high CR and excellent wide viewing properties, because this mode can present the completely black state even under the structure deformation without additional off-axis optical anisotropy. In particular, due to the efficient black state of the OI-NDLC, which is critical for improving the display visibility, the OI phase induced by the NDLC has several advantages over other OI LC modes such as relatively structurally unstable polymer-stabilized blue phase LC (BPLC) modes.[16–19] However, the volume fill-factor of LC nanodroplets, achievable with conventional PIPS approaches, is still too low, which is remains as a critical issue to be elucidated to avail all the unique properties of OI-NDLC mode.[13,20] The low LC fill-factor results in a lower Kerr constant and a higher operation voltage, which must be solved to realize practical applications. Several approaches for improving the EO properties with a higher LC fill factor, have been proposed, including higher LC concentrations, improvement of the mixing ratios of the LC and polymers, and acceleration of the PIPS dynamics.[8] However, previous studies focused only on manipulating material concentrations and the degree of phase separation by improving steps in PIPS. These improvement effects in the LC fill factor are still highly limited.

In this study, we present a more viable approach for preparing the OI-NDLC layer with a higher LC fill factor, where the OI-NDLC phase is reliably achievable by utilizing the nanoporous breath figure (BF) membrane templated by highly self-packed nanosilica spheres. The application engineering of the topologically nanoporous BF membrane structure and novel preparation methods have recently been intensively studied in bioapplications,[21–24] batteries,[25] or fuel cell[26] applications, and chemical or gas sensor[27] applications. In our research, to prepare the densely packed nanosilica sphere layer, the doctor blade coating (DBC) method, which is more suitable for scaling up the colloidal assembly layer than the spin-coating approach, is employed.[28,29] To obtain the nanoporous polymeric membrane as the topologically inverse structure from the highly packed nanosilica layer, a mixture solution of the nanosilica spheres and the UV-crosslinkable monomer is coated through the DBC method. Then, the nanosilica spheres are selectively etched out. For the prepared mixture, the DBC processing parameters such as gap between the substrate and the blade and coating velocity are controlled to obtain a uniform nanoporous membrane template layer with a sufficient thickness for the field-induced Kerr cell condition of the half retarder of the OI-NDLC layer. Two different BF membranes with nanopore sizes of 300 and 500 nm are prepared by adjusting the diameter of the colloidal silica nanospheres. With these nanoporous BF membranes, the OI-NDLC structure can be precisely architectured by infiltrating the LC into the densely packed ordered nanoporous structures. This results in the LC molecules occupying the majority of the volume with a higher fill factor within the sample. Their EO properties and the light scattering and depolarization effects are investigated in detail herein. The Kerr constants for both sample conditions can be much improved compared with those prepared by the PIPS method due to the high fill factor of the NDLCs. Notably, in the case of the 300 nm LC droplet size, an excellent dark state is achievable due to the effectively suppressed depolarization effects of the OI-NDLC phase templated by the nanoporous BF membrane, which is quantitatively analyzed through the imaging polarimetry method.[30–32] Furthermore, the sufficiently suppressed depolarization and scattering loss effects in the presented OI-NDLC condition much improved the light transmittance level together with the resulting CR properties. The presented fabrication method of the OI-NDLC structure templated by the nanoporous BF membrane has the potential for application in flexible LCD modes.

2. Experimental Section

2.1. Preparation of the Mixture of the Colloidal Silica Nanosphere and the Photocrosslinkable Monomer

In the approach, the highly packed nanosphere structure obtained through the DBC method was employed to prepare the nanoporous BF membrane after the selective etching out of the nanospheres. The densely packed nanosphere structure will be inversely templated by the photocrosslinked polymer membrane to obtain the OI-NDLC phase by LC filling into the nanoporous BF membrane. Thus, a well-dispersed mixture solution of the colloidal silica nanospheres and the photocrosslinkable monomer must be prepared. In this study, a sphere-shaped nanosilica colloidal produced by diluting tetraethyl orthosilicate (TEOS) into an ethanol solution was utilized for the BF membrane fabrication.[33] This prevented the formation of undesired silica colloidal sizes and improved the yields of the monodisperse silica spheres of homogeneous shapes and sizes through faster growth dynamics. The nanopore size and its distribution were determined by the colloidal silica nanospheres, their packing density, and uniformity; therefore, synthesizing a nanoscale sphere with a consistent particle size and shape is a critical parameter for creating a highly uniform porous membrane providing a higher LC fill factor condition.

300 nm- and 500 nm-diameter monodispersed silica colloidal nanospheres were synthesized by adjusting the TEOS concentration in a mixture of ethanol and ammonia to investigate the EO and the depolarization effects of the LC nanodroplet sizes determined by the nanoporous BF membrane. To synthesize the 300 nm diameter colloidal silica nanospheres, 46 mL ethanol (Sigma-Aldrich, Inc., ≥99.5%, analytical reagent) was mixed with 10 mL ammonia (Sigma-Aldrich, 13.7 M, analytical

reagent) in a flask. Subsequently, 1 mL diluted TEOS (Sigma-Aldrich, Inc., 98%, analytical reagent) was added, maintaining the relative volume ratio of ethanol to four times with respect to the diluted TEOS amount under rapid stirring at 150 rpm. Next, the mixture was allowed to react at room temperature for 2 h. For the 500 nm diameter colloidal silica nanospheres, the silica growth reaction was performed under a 4 mL increased TEOS concentration condition.

To prepare the mixture solution with the colloidal silica nanospheres and the photocrosslinkable monomer, the colloidal silica nanosphere solution was rinsed and washed out six times in absolute ethanol to remove the unreacted TEOS and the ammonia solvent. This was followed by repeated centrifugation and redispersion. The purified colloidal silica nanospheres were recentrifuged and redispersed in ethoxylated trimethylolpropane triacrylate (ETPTA, SR454, Sartomer), a photocurable monomer that acts as a polymer network in the BF membrane.[34] In addition, 3 wt% of Irgacure 184 was added as a photoinitiator and thoroughly mixed using a vortex mixer, which initiated a radical polymerization through the cross-linking of the monomer molecules upon UV light exposure. Importantly, the prepolymer selection was done based on the refractive index matching with the employed LC. The final mixture was obtained by naturally vaporizing the residual ethanol within the solution for 1 day under dark storage conditions. Its dispersion state was stable for at least a few weeks.

2.2. DBC Method for the Nanoporous BF Membrane

The highly packed colloidal silica nanosphere layer, where the photocrosslinkable monomers were filled between the nanospheres without disturbing the colloidal silica packing ordering, was made through the DBC technique utilizing the shear-driven flow occurring at a tiny blade gap.[35,36] The homogeneous mixture solution of the colloidal silica nanospheres and the photocrosslinkable monomers was highly viscous, but was under a still diluted state, where the colloidal silica nanospheres were randomly dispersed within the mixture solution. However, when a sufficient shearing force was applied to the viscous mixture by moving the 90° doctor blade horizontally and dragging the solution between the tiny blade gap (d_g) (**Figure 1**a), the induced shear stress caused by the shearing force exerted on the colloidal mixture allowed for the fine control of the silica nanoparticles assembly from the prepolymer solution. The induced shear stress (τ) is represented as Equation (1):[36]

$$\tau = -\eta_m \frac{dv_x}{dy} = k\left(\frac{dv_x}{dy}\right)^n, (n < 1) \quad (1)$$

where, η_m is the mixture viscosity; dv_x/dy is the shear strain rate (v_x: velocity of the substrate or blade along the shearing x direction; y: distance from the substrate); k is the material-dependent

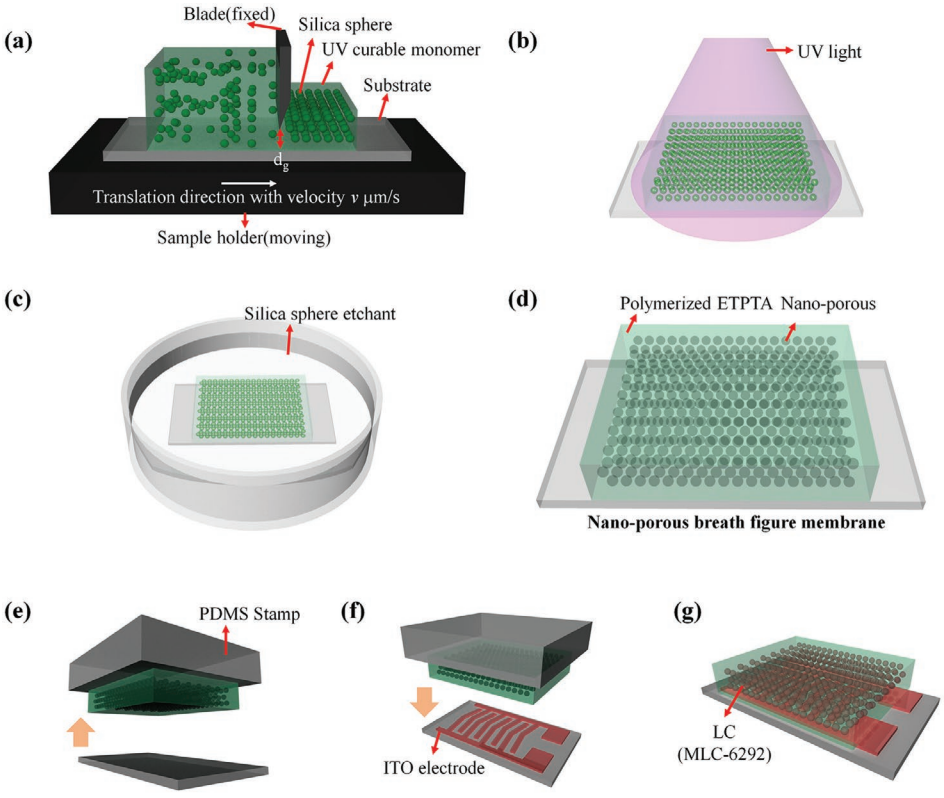

Figure 1. Schematic diagram of the fabrication process for the optically isotropic nanodroplet liquid crystal (OI-NDLC) mode templated by the nanoporous breath figure (BF) polymeric membrane. a) Preparation of the highly packed nanosilica sphere layer by the doctor blade coating, where d_g refers to the gap between the blade end and the substrate. b) ETPTA polymerization by UV irradiation. c) Etching out nanosilica spheres. d) Nanoporous BF polymeric membrane on the donor substrate. e) Pick-up process of the nanoporous BF membrane. f) Transfer process to the device substrate with the patterned ITO electrodes for in-plane-switching (IPS). g) LC filling into the nanoporous ETPTA BF membrane and the final OI-NDLC device structure.

constant; and n represents the deviation level from a Newtonian fluid. As the shear rate increases, the viscosity of the silica colloidal–ETPTA nanocomposite dramatically drops. These shear-thinning effects of the shear-driven pseudoplastic flow can make tightly packed and well-aligned silica nanosphere arrays after passing through the confined area. Therefore, silica colloidal–ETPTA nanocomposites can be fabricated with a high packing density by optimizing the mixture viscosity, blade coating velocity, and gap between the blade and the substrate.

Figure 1 depicts a schematic diagram of the fabrication process sequences for obtaining highly packed silica nanosphere arrays filled with photocrosslinkable monomers, nanoporous BF membranes, and in-plane-switching (IPS)-driven OI-NDLC mode device. The prepared mixture was placed on one sidewall of the 90° doctor blade. The substrate was moved horizontally in our experiment at a controlled speed to obtain the optimum thickness and packing density of the nanocomposite layer of the ETPTA-filled highly packed silica nanosphere array using the induced shearing force effect. The properties of the silica nanosphere membrane depending on the coating velocity and the blade gap condition between the blade and the substrate will be discussed in the next section. Figure 1b illustrates the photo-polymerization of the ETPTA matrix under UV irradiation (365 nm, 30 mW cm^{-2}) for 20 s. During this step, the dense polymer network surrounding the silica nanospheres was formed in the inverse structure of the tightly packed silica nanosphere arrays. The nanoporous BF membrane was obtained by selectively etching out the silica nanospheres from the composite membrane with the aqueous hydrofluoric (HF) acid solution (2% volume fraction) for 30 min (Figure 1c). Subsequently, the prepared nanoporous BF membrane template of Figure 1d was rinsed with deionized (DI) water to remove the residual HF acid. It was then dried in a nitrogen stream.

2.3. OI-NDLC Film Preparation by LC Filling into the BF Membrane

The nanoporous BF membrane was prepared on the nondoped silicon (Si) wafer and it was picked up and transferred to the glass device substrate with the chevron-like interdigitated indium tin oxide (ITO) electrodes prepared for the IPS operation of the OI-NDLC mode by the horizontal fields. Unlike the glass substrate that is vulnerable to the HF acid, the nondoped Si wafer surface is HF-resistive during the selective etching out the process of the silica nanospheres for the nanoporous BF membrane preparation. In addition, the very low surface roughness condition of the Si wafer is advantageous in obtaining the highly packed silica nanosphere array structure by the employed DBC process. Thus, the nondoped Si wafer was used as the donor substrate for the nanoporous BF membrane preparation before transferring it to the glass substrate. For the transfer printing process of the nanoporous BF membrane shown in Figure 1e,f, the viscoelastic properties of the elastic polydimethylsiloxane (PDMS) stamp mold were utilized by controlling the pick-up and transfer-loading velocities of the elastic stamp in transfer printing process.[37] In case of the OI-NDLC mode, operation by using vertically switching electric fields is not proper because the field-induced uniaxial birefringence optic axis formed along the light propagation direction cannot vary incident polarization. Thus, the field-induced birefringent axis needs to be formed along the horizontal direction by the in-plane fields operated by the in-plane patterned IPS electrodes as shown in Figure 1f. The width and spacing of the photolithographically patterned interdigitated ITO electrodes were 3 and 6 μm, respectively. The angles of the chevron-like IPS electrode were ±45° to the transmission axis of the bottom polarizer to obtain a higher light transmittance level with a wider viewing angle properties. Before transferring the nanoporous BF membrane, the planarization layer of polyimide (PI) was spin-coated on the ITO-patterned device substrate. Due to the good insulating properties, the PI layer coated on the interdigitated ITO patterns can improve the voltage holding properties during the IPS operation by preventing the current leakage, inducible by the field-responsive ionic impurities within the LCs, between the common and switching pixel electrodes formed on the same substrate plane.[38]

Finally, a nematic LC (NLC) of MLC-6292 ($\varepsilon_{\parallel} = 11.1$, $\varepsilon_{\perp} = 3.7$, $\Delta\varepsilon = 7.4$ at 1 kHz and 20 °C; $n_e = 1.56$, $n_o = 1.47$, $\Delta n = 0.09$ at $\lambda =$ 589.3 nm and 20 °C) was filled into the nanoporous polymeric membrane at a temperature above the nematic–isotropic transition of MLC-6292 ($T_{NI} = 120$ °C) to obtain an ideally isotropic NDLC phase and avoid LC ordering effects by the anisotropic fluid of the nematic phase. Considering the refractive index of the polymerized ETPTA ($\varepsilon_p = 3$; $n_p = 1.47$), the NLC was chosen to suppress the scattering loss induced by the refractive index mismatching between the LC nanodomains and the polymeric backbone structure. Importantly, the flow viscosity level of the NLC was also considered for an efficient capillary filling of the NLC through the nanoporous polymeric membrane network. The flow viscosity coefficient (28 mm^2 s^{-1} at 20 °C) of the MLC-6292 was sufficiently low, even for the 300 nm sized pores of the BF membrane. Compared to the room temperature, the elevated temperature condition over T_{NI} employed for the LC filling procedure might help in achieving an efficient LC infiltration through the nanoporous membrane at a lower-LC viscosity condition than that at room temperature. Figure 1**g** depicts the final structure of the OI-NDLC mode templated by the nanoporous BF membrane, where the transmission axis of the top analyzer was set to be orthogonal to that of the bottom polarizer.

2.4. Methods of the Electro-Optic Kerr and Depolarization Effects

To evaluate the EO characteristics from the measurements for display applications, the achievable maximum light transmittance level of the OI-NDLC mode was analyzed as follows considering the device structure and assuming that the depolarization effects are negligible:

$$T_{LC} = \sin^2 2\psi \sin^2\left(\frac{\pi \Delta n_{eff} d}{\lambda}\right) \tag{2}$$

$$T = T_{ar} \times \frac{1}{2} T_{LC} \tag{3}$$

where ψ is the relative angle between the incident light polarization axis and the field-induced LC director orientation; Δn_{eff} is the effective field-induced birefringence of the LC; d is the cell thickness; λ is the incident light wavelength; T_{LC} is the transmittance factor caused by the field-induced in-plane retardation of the OI-NDLC layer; and T_{ar} is the transmittance loss factor represented as the effective pixel aperture ratio. In our experiment, ψ is ±45°, as explained in Figure 1f. The T_{LC} level was determined by the field-induced retardation amount of the OI-NDLC layer. The in-plane electric fields were effectively applied at the regions between the interdigitated IPS electrodes; hence, the NDLC layer on the patterned ITO electrodes remained in the optically isotropic state, irrespective of the applied voltage levels as shown in Figure S1 (Supporting Information). Thus, the incident beams traveling these regions were blocked under the crossed polarizers. Considering the photolithographically patterned IPS ITO structure in our experiment, the T_{ar} level was less than 67% and can be further improved by employing finer IPS electrode patterns. Considering current industry manufacturing levels, the ITO pattern width for the IPS operation can be reduced to 2 µm, which corresponds to the improved T_{ar} level of 75% from 67% in our experiment for a higher transmittance of the OI-NDLC mode. In the OI-NDLC phase comprising randomly oriented NDLC encapsulated by the nanoporous membrane, the field-induced birefringence can be explained by the Kerr effect showing the quadratic relationship between the applied electric field (E) and the Δn_{eff} amount:[39,40]

$$\Delta n_{eff} = \lambda K_{Kerr} E^2 \tag{4}$$

$$\Delta n_{eff} = \Delta n_s \left\{ 1 - \exp\left[-\left(\frac{E}{E_s} \right)^2 \right] \right\} \tag{5}$$

where K_{Kerr} (m V^{-2}) is the Kerr constant, Δn_s is the saturated birefringence and E_s is the saturated applied electric field. The Δn_{eff} equals to Δn_s as the E reaches E_s. A field-induced ordering of the polar molecules in the optically isotropic medium causes the Kerr effect. **Figure 2** shows the schematic of the LC molecule orientations under the nanodispersed LC droplet states templated by the nanoporous BF membrane plotted according to the applied field conditions. As shown in Equations (2)–(5), in the absence of the applied field, an ideal dark state is achievable, irrespective of the incident angle and the cell gap variation, which are the most desirable features of the OI-NDLC mode for flexible display applications. The total transmittance level gradually increased with the increasing applied in-plane fields due to the field-induced Kerr effects of Δn_{eff}. However, as shown in Figure 2b and Figure S2a (Supporting Information), the effective in-plane field amounts between the interdigitated ITO electrodes patterned at the bottom substrate gradually decreased towards the top surface of the OI-NDLC layer and far from the underlying substrate. The average electric field amount of E was lower than the electric field near the bottom substrate (Figure S2a, (Supporting Information)); thus, the field-induced NDLC Kerr effects of Δn_{eff} near the bottom substrate became saturated first as the achievable maximum

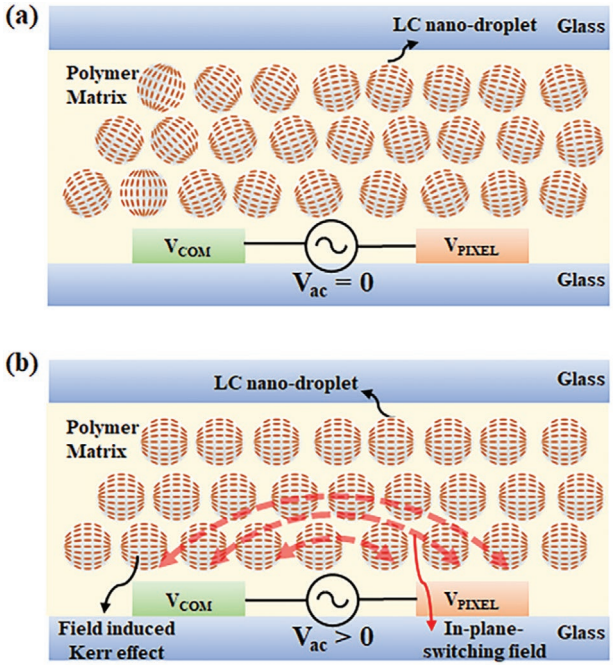

Figure 2. Schematic diagram of the LC molecule orientation in the dispersed LC nanodroplets templated by the nanoporous BF membrane depending on the electric field condition: a) optically isotropic nanoencapsulated LC state at the field-off condition and b) field-induced anisotropic Kerr LC cell state at the field-on condition. V_{COM} and V_{PIXEL} are the IPS electrodes for the IPS operation, where V_{COM} denotes common electrodes; V_{PIXEL} represents pixel electrodes; and V_{ac} is applied voltage.

amount of Δn_s. The effective field-induced Δn_{eff} amount also gradually decreased as it approached the top substrate. For a higher light transmittance, the retardation achievable by the field-induced Δn_{eff} and the device condition of the cell gap (d) must meet the half retarder condition. To reduce the operation voltage, the development of a higher Kerr constant is essentially required in the material aspect of the OI-NDLC phase, and the adoption of a finer interdigitated electrode spacing is desirable in the device structure.

The scattering loss and consequent depolarization effects of the OI-NDLC phase must be analyzed to more precisely characterize the achievable darkest and brightest levels of the OI-NDLC mode. During the beam propagation through the OI-NDLC cell layer, the ray scattering accompanying the depolarization effects can induce the light leakage for the darkest state under the on- and off-axis viewing conditions and those effects also result in an actual transmittance level for the brightest state that would be lower than the ideal T value in Equation (3). Consequently, the CR level of the OI-NDLC mode might degrade, which is an undesirable effect that needs to be avoided in the perspective of practical display applications. The scattering-induced beam patterns and their degree-of-polarization (DOP) maps were measured by using the imaging polarimetry optics to analyze the depolarization effect of our OI-NDLC devices.[41]

Figure 3 depicts the experimental setup for characterizing the scattering-induced depolarization effects of the prepared OI-NDLC cells according to the LC nanodroplet size variation. A normally incident linearly polarized He–Ne laser (at λ = 632.8 nm)

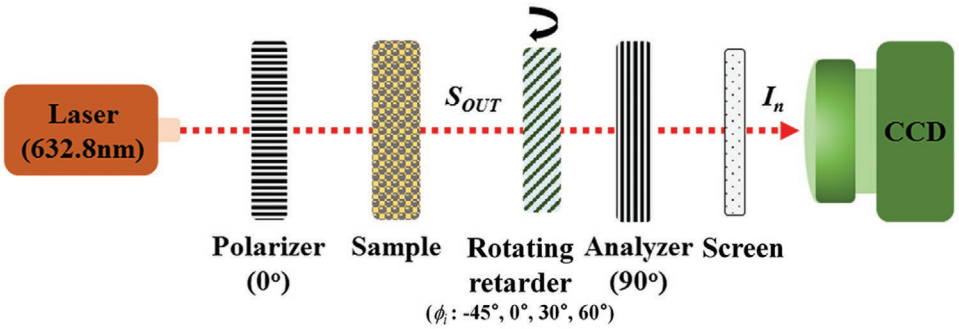

Figure 3. Experimental optical setup for characterizing the degree of polarization levels induced by light scattering and depolarization effects of the optically isotropic nanodroplet liquid crystal phases according to the BF membrane preparation conditions.

was used as a light source in the imaging polarimetry measurement. In sequence, the incident laser beam passed through the polarizer set at 0° transmission axis, the prepared OI-NDLC cells templated by the BF membrane with different LC droplet sizes, the rotatable $\lambda/4$ retarder, and the analyzer (90° transmission axis). The polarization states after passing through the OI-NDLC samples were modulated by rotating the $\lambda/4$ waveplate with the four steps (i.e., $\phi_i = -45°$, 0°, 30°, and 60°). The final transmitted light was displayed onto the semitransparent screen. Scattered intensity beam patterns were acquired by the CCD through an objective lens while varying the ϕ_i conditions of the quarter waveplate (Figure 3). From the gray intensity maps ($I_i(x,y)$; i = 1, 2, 3, and 4) obtained at four different ϕ_i conditions, the DOP state distribution of the DOP(x,y) right after the OI-NDLC cells can be analyzed using the Stokes vectors, $S_{OUT}(x,y)$ through a 4 × 4 Muller matrix (Equations 6–8):[30,42]

$$S_{OUT} = \begin{pmatrix} S_0 \\ S_1 \\ S_2 \\ S_3 \end{pmatrix} = (M_{PSA})^{-1} \begin{pmatrix} I_1 \\ I_2 \\ I_3 \\ I_4 \end{pmatrix} \tag{6}$$

where, the 4 × 4 Muller matrix of M_{PSA} was experimentally obtained as follows:

$$M_{PSA} = \frac{1}{2} \cdot \begin{pmatrix} 1 & -\cos^2(2\phi_1) & -\sin(4\phi_1)/2 & \sin(2\phi_1) \\ 1 & -\cos^2(2\phi_2) & -\sin(4\phi_2)/2 & \sin(2\phi_2) \\ 1 & -\cos^2(2\phi_3) & -\sin(4\phi_3)/2 & \sin(2\phi_3) \\ 1 & -\cos^2(2\phi_4) & -\sin(4\phi_4)/2 & \sin(2\phi_4) \end{pmatrix} \tag{7}$$

Finally, the DOP(x,y) map according to the scattering-induced depolarization effects by the LC nanodroplet conditions was obtained as follows using the positional Stokes parameters derived from Equation (6) and (7):[43]

$$\mathrm{DOP}(x,y) = \frac{\left(S_1^2 + S_2^2 + S_3^2\right)^{1/2}}{S_0}, (0 \le \mathrm{DOP} \le 1) \tag{8}$$

The DOP values of 0 and 1 indicate the completely depolarized (i.e., nonpolarized) and perfectly polarized lights, respectively. The DOP value between 0 and 1 represents the transmitted beams becoming the partially polarized state from the initially perfect polarization after passing through the OI-NDLC cells. If the depolarization effects by the OI-NDLC cells are negligible, the polarization state might be changed by the field-induced Kerr effects from the linear polarization of the initial state; however, the DOP level (≈1) remains unperturbed by the distributed LC nanodroplets.

3. Results and Discussion

3.1. Synthesized Colloidal Silica Nanospheres with Difference Sizes

The synthesis process of the colloidal silica nanospheres of two different sizes (D_{LC}) (i.e., 300 and 500 nm) was performed in our experiments to investigate the effects of the EO properties of the OI-NDLC phase according to the size of the LC droplets infiltrated within the nanoporous BF membrane. As shown by the scanning electron microscopy (SEM) images in **Figure 4**a,b, the monodisperse states of the sphere-shaped silica nanoparticles could be obtained well for both diameter conditions by controlling the relative volume ratio of the TEOS and ethanol during the colloidal silica synthesis reaction. With the solvent-vaporized state, the SEM images showed densely packed silica nanosphere arrangements with a high uniformity of the silica diameters.

3.2. DBC Control for the Nanoporous BF Membrane

Our ultimate goal is to make an OI-NDLC phase for better EO properties. Accordingly, the thickness and the distribution uniformity of the nanoporous polymer membrane and the high filling factors (packing density) of the NDLC must be achieved for superior EO properties. Especially for the higher light efficiency of the OI-NDLC mode as the display applications, these features must be met at a sufficiently thick nanoporous membrane condition as required for the field-induced Kerr cell of the $\lambda/2$ retardation. In the DBC method, the film thickness and the fill factor of the nanopores within the BF membrane are highly dependent on the coating conditions, such as the gap between the blade and the substrate and the coating velocity.

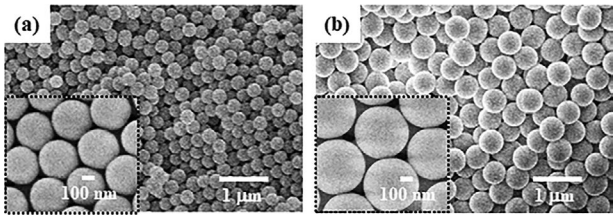

Figure 4. Scanning electron microscopy (SEM) images of the synthesized silica colloidal spheres with a) 300 nm and b) 500 nm of the average diameters (D_{LC}). The insets show the magnified SEM images for each case.

For the mixture solution of the synthesized silica nanospheres and the UV-crosslinkable ETPTA, the coating conditions were optimized to improve the OI-NDLC mode in our experiment.

3.2.1. Thickness and Packing Density Control with the Gap between the Blade and the Substrate

Under the fixed coating speed condition of 4 μm s^{-1}, the achievable thickness condition after the DBC preparation of the silica–ETPTA nanocomposites was first investigated by varying the blade gap (d_g). In **Figure 5**, the average thickness of the silica–ETPTA nanocomposite film obtained by the DBC method increased as the blade gap condition decreased because of the enhanced flow of the silica–ETPTA nanocomposite mixture at a narrower blade gap caused by the shearing force, where the sufficiently thick silica–ETPTA nanocomposite layer was achievable at the blade gap condition of $d_g \leq 2$ μm. The smaller gap between the blade and the substrate provided favorable conditions for controlling the selective flow and the subsequent self-packing of the silica nanoparticles (Figure 5). As a result, the film uniformity along the membrane thickness improved much as the blade gap condition decreased within our experimental regime. In the other aspects of the packing density of the silica nanospheres, the silica nanospheres encapsulated by the UV-crosslinked ETPTA matrix obtained at the $d_g = 1$ μm condition also showed the most tightly packed structure (Figure 5a–d).

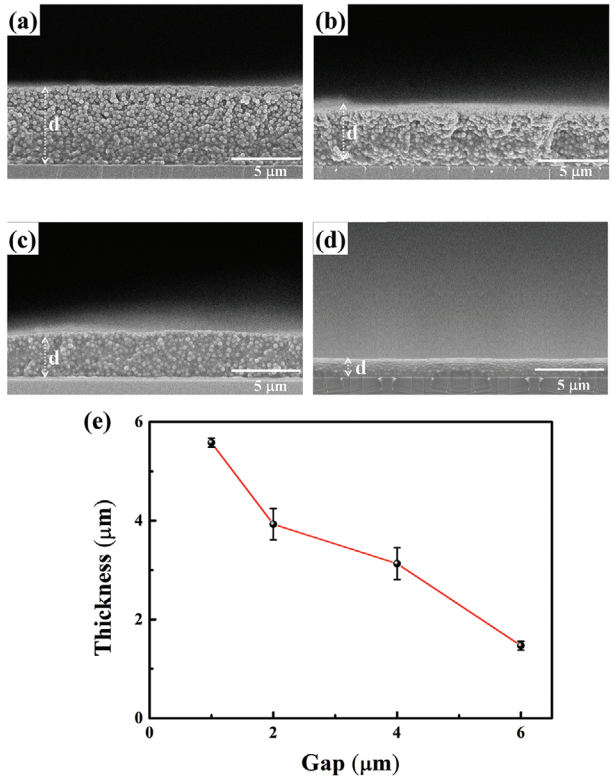

Figure 5. Cross-sectional SEM images of the silica–ETPTA nanocomposite layers ($D_{silica} \approx 300$ nm) prepared by the doctor blade coating (DBC) method, where the DBC condition of d_g is controlled by a) 1 μm, b) 2 μm, c) 4 μm, and d) 6 μm. *d* represents the average film thickness. e) Thickness of the coated colloidal particle–ETPTA nanocomposite layer depending on the d_g conditions.

3.2.2. Thickness and Packing Density Control with the Coating Velocity

Based on previous discussions on the shearing force effects of the blade gap condition on the silica–ETPTA nanocomposite layer properties, the coating velocity effects during the DBC procedure were investigated herein under the fixed condition of $d_g = 1$ μm (**Figures 6** and **7**). The coating thickness of the silica–ETPTA nanocomposite layer exhibited a large variation according to the coating velocity, where the film thickness increased as the coating velocity decreased. The average film thicknesses of $d \approx 10.5$ and 0.4 μm were obtained at the coating velocities of 2 and 8 μm s^{-1}, respectively. **Figure 8** presents the shear-induced flow velocity profiles below the doctor blade according to the blade moving velocity as a schematic diagram depicted in terms of the pressure force–viscous force ratio (Π).[44,45] When the blade speed was too fast, the viscous force was dominant over the pressure force (Π << 1 regime in Figure 8a), and a thinner coating layer was obtainable(Figures 6d and 7). In our experiment, the average film thickness of the silica-–ETPTA nanocomposite layer was even thinner than the blade gap of d_g at the 8 μm s^{-1} coating velocity. On the contrary, at the Π >> 1 regime obtainable when the blade speed was too slow, the pressure force by the coating blade became dominant over the viscous force, and a film thicker than the blade gap can be achieved (Figure 8b). The experimental results in Figures 6 and 7 show the same tendencies of the coated silica–ETPTA nanocomposite layer becoming thicker as the coating velocity became slower. However, as shown in the cross-sectional SEM image in Figure 6a obtained at the 2 μm s^{-1} coating velocity, the loosely packed nanosphere structure was obtained after blade coating when the hydrostatic pressure became the dominant flow mechanism at the blade gap. To obtain the highly packed nanosphere structure by minimizing the ETPTA encapsulating matrix and by achieving a sufficiently thick layer, the balancing condition between the pressure and viscous forces must be searched for during the shearing force-induced blade coating. Considering the film properties of the coated silica–ETPTA nanocomposite (e.g., achievable thickness and its uniformity and nanosilica packing density), the blade coating velocity of 4 μm s^{-1} was chosen at $d_g = 1$ μm in our experiment.

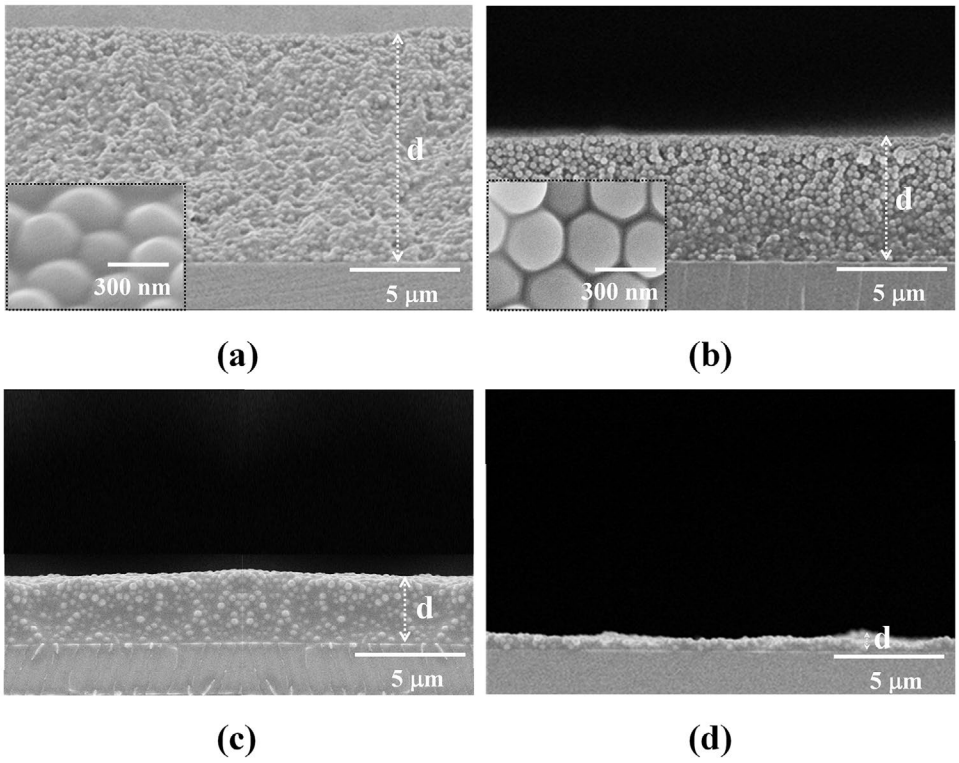

Figure 6. Cross-sectional SEM images of the silica–ETPTA nanocomposite layers ($D_{silica} \approx 300$ nm), where the DBC condition of the coating velocity is controlled by a) 2 μm s^{-1}, b) 4 μm s^{-1}, c) 6 μm s^{-1}, and d) 8 μm s^{-1}. *d* represents the average film thickness. The insets show a magnified silica–ETPTA nanocomposite.

3.2.3. Nanoporous BF Membrane Template for the OI-NDLC Mode

Figure 9 shows the cross-section SEM images of the nanoporous BF membrane obtained after the selective etching out of the silica nanospheres from the silica–ETPTA nanocomposite layer ($D_{silica} \approx 300$ nm) obtained using the DBC method. After the selective silica etching with the aqueous solution of HF acid, the UV-crosslinked ETPTA polymeric matrix showed highly porous honeycomb networks, which had a 3D inverse structure of the densely packed silica nanosphere arrangement before etching. The cross-sectional SEM image of Figure 9a shows that the nanohole arrangement of the nanoporous BF membrane has a well-aligned hexagonal packing structure though it can be observed somewhat differently depending on the sampled cross-sectional view. The hexagonal arrangement of the nanoholes of the BF membrane can also be confirmed from the enlarged SEM image of Figure 9b, where the triangular-arranged holes formed for the cross-connections between the hexagonally arranged layers are clearly observable within the dotted circle. When we estimated the average distance between the nanohole centers of the nanoporous BF membrane after sampling out the SEM image area where the hexagonal nanohole arrangements are properly observed, the average nanohole period was about 317.4 nm with the standard deviation of ±2.7 nm. This estimation corresponded to the 66.1% of the volume fraction of the nanopore regions and only 33.9% of the volume was filled by the ETPTA networks. With the proposed method, the LC volume fill factor of approximately 66.1% by the LC nanodroplets was achievable. When we re-estimated the 2D LC fill factor by following the previous reports, the LC volume fill factor of 66.1% corresponded to the 2D LC fill factor of 58% in our work, which was significantly higher than the previously reported achievements (<48% in the 2D LC fill factor) of the OI-NDLCs obtained through the conventional PIPS methods.[46–48]

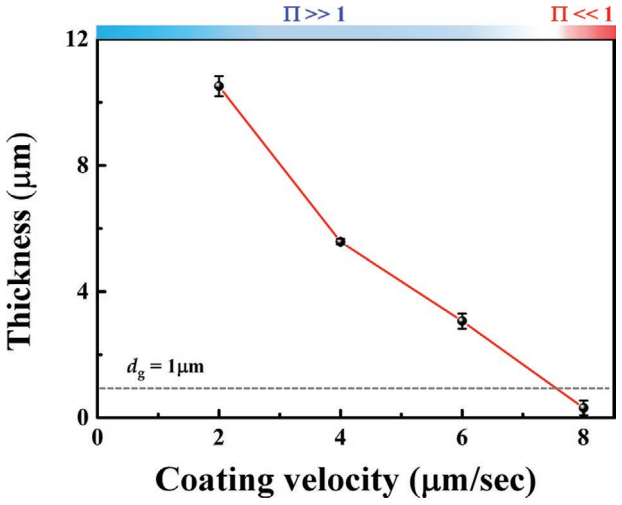

Figure 7. Thickness (*d*) of the DBC-prepared colloidal nanoparticle–ETPTA nanocomposite layers depending on the coating velocity.

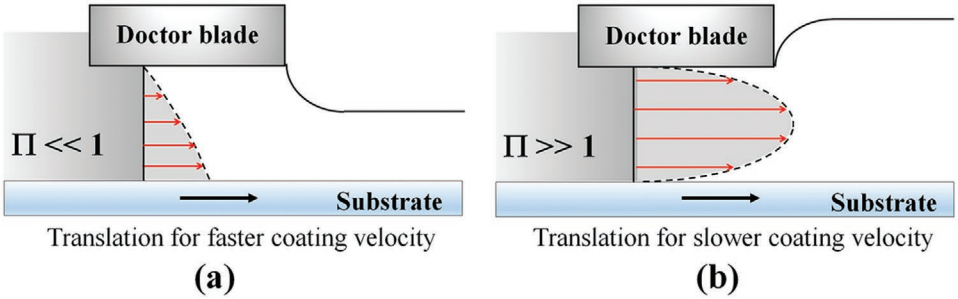

Figure 8. Schematics of the DBC mechanisms depending on Π that is the relative ratio between the pressure force and viscous force: a) Π << 1 and b) Π >> 1, which correspond to the thinner and thicker highly packed nanosilica layers obtainable at faster and slower doctor blade moving velocity conditions, respectively.

3.3. EO Properties and Depolarization Effects Depending on the LC Droplet Sizes of the OI-NDLC

For the nanoporous BF membranes transferred to the device substrates with the patterned IPS ITO electrodes, the NLC of MLC-6292 was infiltrated into the nanopores, as explained in Section 2.3. In terms of the LC nanodroplet diameters ($D_{LC} \approx 300$ and 500 nm), two types of OI-NDLC cells were prepared by utilizing the self-packing effects of the DBC method. Before characterizing the EO properties of the OI-NDLC cells, the scattering-induced depolarization levels of the OI-NDLC cells initially at the field-off state were evaluated for both samples with the 300 nm and 500 nm LC nanodroplets by using the imaging polarimetry measurement shown in Figure 3. **Figure 10**a shows the four CCD image sets of the scattered intensity beam patterns projected onto the semitransparent screen with varying ϕ_i conditions of the quarter waveplate. For the same sample, the scattered intensity beam patterns acquired after the analyzer were changed depending on the ϕ_i condition. The DOP(x,y) maps in Figure 10b were extracted from the image sets of the two types of OI-NDLC cells using Equations (6)–(8). The bright centered spot was associated with the light transmitted without scattering; hence, we evaluated the DOP levels, except for the center regions, for comparative studies on the depolarization effects of the scattering-induced off-axis rays according to the D_{LC} conditions. The DOP(x,y) gray maps in Figure 10b clearly indicate that the depolarization effects by the scattered off-axis rays were weaker in the OI-NDLC sample with $D_{LC} \approx 300$ nm than that with $D_{LC} \approx 500$ nm. In the scattered beam intensity patterns shown in Figure 10a, the spatially fourfold symmetry is observable because the light transmittances by the scattering-induced off-axis rays are higher along the transmission axis directions of the crossed polarizers (0° and 90° in our imaging polarimetry measurement shown in Figure 3). Because of the stronger off-axis ray scattering at the increased LC nanodroplet condition, this fourfold symmetry intensity pattern is more enhanced in the OI-NDLC sample with $D_{LC} \approx 500$ nm than that with $D_{LC} \approx 300$ nm. However, the final DOP maps showed the angular symmetric distribution of the depolarization levels for both samples as shown in Figure 10b, which means that the DOP analysis extracted from the four sets of the measurements correctly results in the scattering-induced depolarization effects according to the LC nanodroplet size condition while excluding the spatially nonuniform scattering-induced intensity profile effects. A quantitative comparison of the spatial average DOP values from the DOP(x,y) maps showed that the DOP levels for the OI-NDLC samples with the nanodroplet sizes of 300 and 500 nm were 0.85 and 0.80, respectively, showing that the DOP level improved as the LC nanodroplet size decreased. The high DOP levels can also be attributed to our material selection considering the refractive indices of the employed NLC and the polymer matrix for a lower refractive index mismatching.

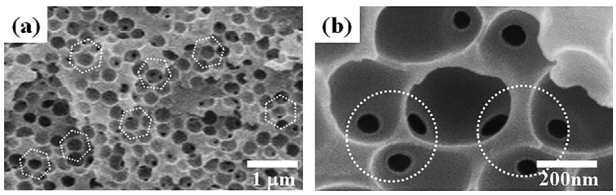

Figure 9. SEM images of the nanoporous BF membrane after selectively etching out the highly packed silica nanospheres from the silica–ETPTA nanocomposite layers ($D_{silica} \approx 300$ nm) prepared through the DBC method. b) is the enlarged image of a).

Figure 11 shows the IPS-driven LC textures of the two types of OI-NDLC samples. The polarizing optical microscopy (POM) images obtained under the field-off and -on conditions for the dark and bright states of the operation modes, respectively, depict that the D_{LC} conditions highly affect the transmittance levels for both operation modes. In Figure 11, V_{max} represents the applying voltage levels required for the maximum transmittances (i.e., for the brightest states) for each sample, as shown in the voltage–transmittance (V–T) curve sets in **Figure 12**a. In the field-off state, the OI-NDLC sample with $D_{LC} \approx 300$ nm exhibited a completely dark state. In contrast, a light leakage was observable in the case of $D_{LC} \approx 500$ nm. In the case of the brightest states by applying fields, the OI-NDLC sample prepared with the smaller D_{LC} condition of ≈300 nm was brighter than that of $D_{LC} \approx 500$ nm.

The quantitative comparisons of the EO properties of the two samples can be provided by the V–T curves shown in Figure 12a. In the field-off state, the light leakage levels (T_{off}) of the OI-NDLC samples were $T_{off} = 0.05\%$ and 0.16% for the $D_{LC} \approx 300$ nm and ≈ 500 nm conditions, respectively, showing an improvement compared to those prepared by the conventional PIPS nano-PDLCs.[49–51] This corresponded to the dark state enhancement effect of the light leakage reduction of 68% in the OI-NDLC sample with $D_{LC} \approx 300$ nm compared to $D_{LC} \approx 500$ nm. The drastic improvement of the dark state

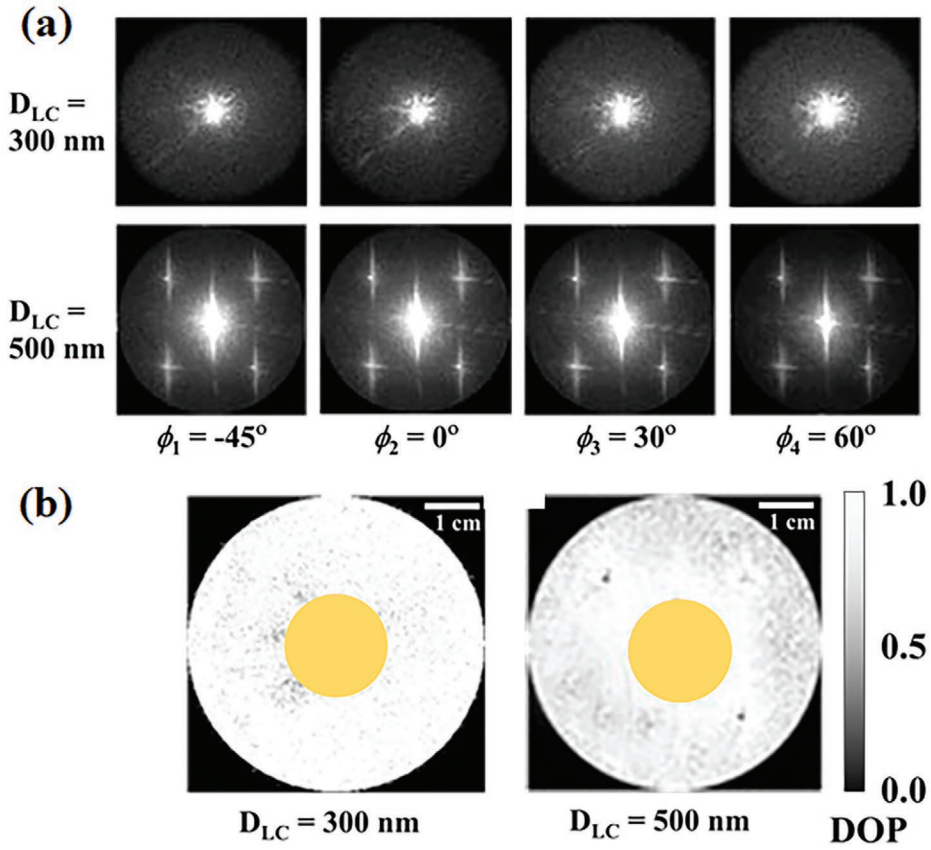

Figure 10. Analysis on the DOP and depolarization effects performed by the scheme of Figure 3. a) Transmission beam profiles of the OI-NDLC devices measured by rotating the retardation axis of the ϕ_i condition for the samples templated with different nanosilica sizes (D_{LC}). b) DOP(x,y) maps analyzed by Equations (6) to (8) from the ϕ_i-dependent transmitted beam profiles. For two samples, the average DOP levels are compared with each other, except for the yellow-circled image center areas, to analyze the depolarization effects of the scattering-induced off-axis rays and avoid the quantitative DOP evaluation errors induced by the beam saturation of the on-axis optical rays.

is attributed to the reduced light scattering and depolarization effect under the decreased D_{LC} condition. The results showed that the D_{LC} condition significantly affected the scattering-induced dark state. The dark state obtained in the OI-NDLC sample with $D_{LC} \approx 300$ nm could be maintained, irrespective of the viewing direction, due to the optically isotropic nature in the field-off state in contrast to most of the LC modes exhibiting the optically anisotropic phase in the field-off state. Compared with twisted nematic (TN) LC modes requiring complex and expensive compensation films,[52–54] IPS LC modes utilizing field-induced LC director switching along the horizontal directions are known to be advantageous in obtaining symmetric and wide viewing angle characteristics. But, because of the optical uniaxial property, the small angle of the surface pretilt of the LC alignment layer can asymmetrically distort the off-state viewing angle property with degrading the CR symmetry even in the IPS LC modes, which should be resolved.[55–58] Whereas, the presented OI-NDLC mode can exhibit superior and symmetric wide viewing angle properties because the retardation-induced polarization change, as shown in Equations (2) and (4), does not occur irrespective of viewing directions at the field-off optically isotropic state.[14,15]

In the field-on state, the V_{max} condition for the maximum bright levels was higher in the OI-NDLC mode with $D_{LC} \approx 300$ nm (i.e., $V_{max} \approx 142.5$ and 120.0 V for the $D_{LC} \approx 300$ and 500 nm conditions, respectively). Like in the conventional PDLCs made by the PIPS methods, the LC molecules near the polymer matrix were relatively hard to reorient in response to an applied field because of surface anchoring effects. The relatively increased condition of the surface-to-volume ratio at the reduced D_{LC} condition decreased the Δn_{eff} amount in Equations (4) and (5). This corresponded to the Kerr constant evaluation results for the two types of the OI-NDLC samples. Figure 12b shows the IPS field-induced Δn_{eff} plotted against the squared electric field (E^2), which were obtained from the normalized V–T curves in Figure 12a. In evaluating the Kerr constants, the average values of the horizontal fields, obtained by the numerical simulations (Tech-wiz LCD 3D, Sanayi System, Co., Ltd., South Korea), were used according to the applied voltages for considering the gradually decreasing behaviors of the depth field profiles from the bottom to top surfaces (Figure S2, Supporting Information). As the dielectric constant condition of the OI-NDLC layer for the simulation, the average value of $\varepsilon_{avg} = 5.15$ was assumed by considering the dielectric constants of the NLC and ETPTA polymer, and their volume fractions.

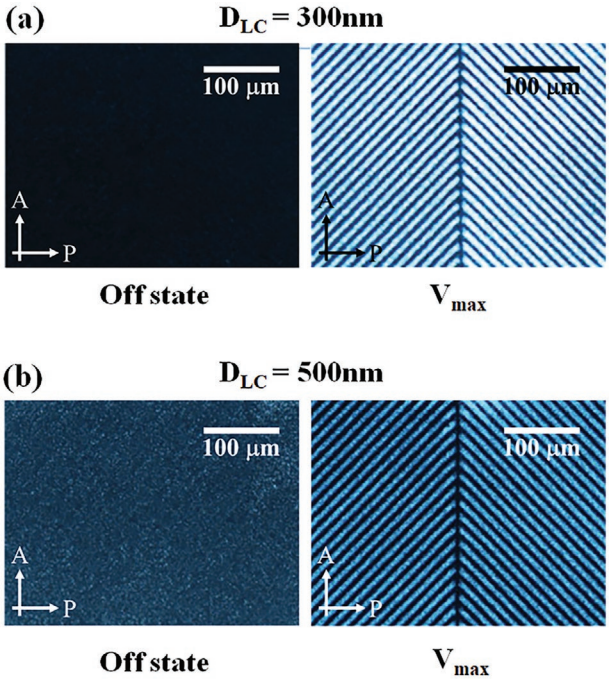

Figure 11. Polarizing optical microscopy images of the OI-NDLC mode cells templated by different nanosilica spheres of a) $D_{LC} \approx 300$ nm and b) $D_{LC} \approx 500$ nm. The first and second images in each figure set are the POM LC textures at the field-off and field-on states, respectively, measured under the condition of the crossed polarizers. *P* and *A* correspond to the transmission axis of the bottom polarizer and the top analyzer, respectively. The POM images for the bright state are obtained by applying V_{max} that corresponds to the voltage level required for the maximum transmittance level in each cell.

The Kerr constants of the OI-NDLC samples obtained by linear fitting were 5.75×10^{-9} and 9.15×10^{-9} m V^{-2} for the $D_{LC} \approx 300$ nm and ≈500 nm conditions, respectively; thus, the Kerr constant of the OI-NDLC mode with $D_{LC} \approx 300$ nm was slightly lower than that of $D_{LC} \approx 500$ nm. However, in both sample conditions, the achieved Kerr constants were competitive values compared with those of the other OI systems due to the high LC fill factor available with the NDLC preparation templated by the nanoporous membrane.[13,18,59,60] This was about 2600 times higher than that of nitrobenzene ($K_{Kerr} \approx 2.2 \times 10^{-12}$ m V^{-2}) known as a high-Kerr optical material. However, the operating voltage levels presented in this work were still higher than the conventional TN or IPS LC modes. To further improve the operation voltage level, the material condition for a higher Kerr constant needs to be improved even though the Kerr constant of the OI-NDLC mode was much improved by increasing the LC volume fraction with the presented BF membrane template approach. As shown in Equation (5) with the saturated birefringence of Δn_s, the Kerr constant can be improved by adopting an LC with a higher Δn. In our experiment, LC with $\Delta n = 0.09$ was employed. Recently, an LC with $\Delta n \approx 0.4$ has been reported.[61] As an alternative approach at the same LC condition, the Kerr constant can be effectively improved by increasing the dielectric constant of the LC-encapsulating polymeric layer for enhancing the effective fields applied to the LC nanodroplets.[15] By adopting the high *K* nanoparticle–polymer composite material, we have successfully shown that the operating voltage levels can be effectively reduced.[15]

When we compared the maximum transmittance levels (T_{on}) between the two samples (Figure 12d), the improvement effects caused by the reduced depolarization through the adoption of the decreased D_{LC} condition of 300 nm were lower than the light leakage improvement (T_{on} = 10.68% and 9.04% for the $D_{LC} \approx 300$ nm and ≈500 nm conditions, respectively). The T_{on} level of the OI-NDLC sample with $D_{LC} \approx 300$ nm was improved by 18% compared to that of $D_{LC} \approx 500$ nm. In contrast to the field-off state, where the scattered depolarized rays degraded the dark level as the light leakage transmitting through the analyzer increased, the transmittance level by the induced Kerr effects of the polarized beams decreased as the depolarization effects increased, whereas that of the nonpolarized beam increased under the partially polarized condition.[15] In the case of the field-off state, the effective optic axis orientation of the LC nanodroplets was randomly distributed, but the LC molecules were realigned along the in-plane field direction in the field-on state. Under the field-induced optic axis alignment condition of the LC nanodroplets, the beam scattering for the extraordinary rays became higher due to the field-induced increased index mismatching condition between the n_e of the NLC and the n_p of the polymer matrix, which is attributed to the reduced improved effects of the T_{on} levels compared with the T_{off} improvement. However, due to the positive improvement effects of the T_{on} and T_{off} levels after the reduced D_{LC} condition adoption, the CR (T_{on}/T_{off}) level of the OI-NDLC mode with $D_{LC} \approx 300$ nm could be significantly improved by 278% compared to that of the mode with $D_{LC} \approx 500$ nm: CR ≈ 208.6:1 and 56.1:1 for the $D_{LC} \approx 300$ nm and 500 nm conditions, respectively. The achievable CR level is one of the most important characterization factors determining the image visibility of the display panel. The CR level achieved by the OI-NDLC mode templated by the nanoporous BF membrane was quite higher than those obtained by the conventional PIPS approaches.[49–51] With the presented fabrication scheme that can provide the high fill factor of the LC nanodroplet dispersions by utilizing the reliable self-packing effects of the nanospheres, the CR level is expected to be more improved by the further suppression of the light scattering effects with the introduction of the reduced diameters of the nanoparticles in the nanoporous BF membrane preparation.

4. Conclusion

In this study, we demonstrated a self-structured printing approach for the OI-NDLC device based on the nanoporous BF membrane template using the DBC technique that provides uniformly packed dense nanosized LC droplets, at which the LCs are encapsulated by the UV-crosslinked polymer network with a high LC fill factor of approximately 66.1%, resulting in a high Kerr constant of 5.75×10^{-9} m V^{-2}. This technique allowed the OI-NDLC phase to achieve superior EO properties, including an excellently low light leakage level of 0.05% and a CR level of 208.6:1, due to the sufficiently suppressed depolarization effect at the much-reduced LC nanodroplet size of 300 that is templated by self-packed silica nanospheres. Comparing the CR properties of the OI-NDLC sample prepared with the

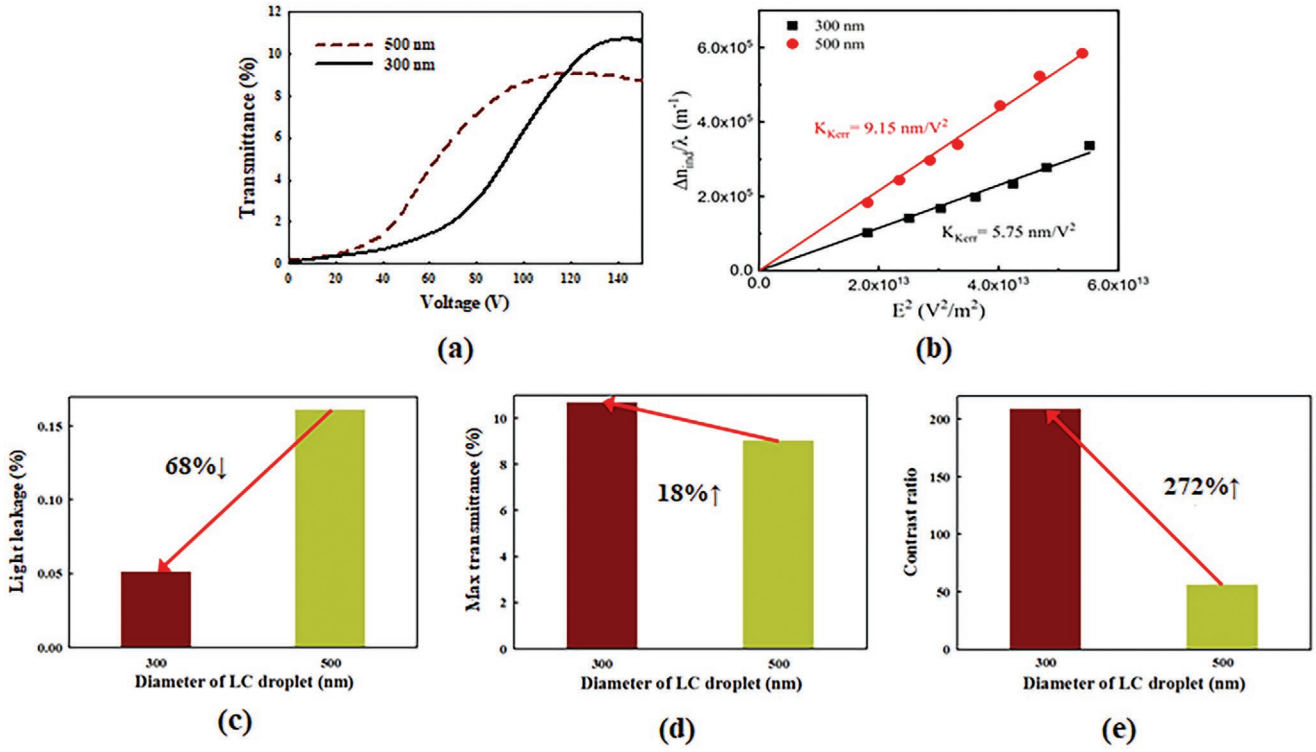

Figure 12. a) Voltage–transmittance curves for the BF-templated OI-NDLC mode cells (the D_{LC} conditions are 300 and 500 nm for comparison). Comparative evaluations on b) the field-induced birefringence levels according to the squared electric field, plotted for the Kerr constant evaluation, c) light leakage levels at the field-off state, d) maximum transmittance levels at the field-on state, and e) contrast ratio (CR) levels.

$D_{LC} \approx 300$ nm condition with that of the $D_{LC} \approx 500$ nm, the achievable CR level can be improved by 278%. The presented DBC technique of utilizing the self-structured nanoporous BF membrane that can reliably provide the OI-NDLC phase in a large-area scalable approach is a promising tool for high-yield and high-performance OI-NDLC mode preparation among several OI-NDLC phase techniques.

Supporting Information

Supporting Information is available from the Wiley Online Library or from the author.

Acknowledgements

Y.-C.S. and J.-S.P. contributed equally to this work. This work was supported by the National Research Foundation of Korea (NRF) grant funded by the Korea government (MSIT) No 2019R1A2C1005531).

Conflict of Interest

The authors declare no conflict of interest.

Data Availability Statement

Research data are not shared.

Keywords

depolarization effects, displays, liquid crystals, nanodroplet liquid crystals, optically isotropic mode

Received: October 5, 2021
Revised: November 24, 2021
Published online: January 27, 2022

[1] J. E. Anderson, P. J. Bos, *Jpn. J. Appl. Phys.* **2000**, *39*, 6388.
[2] S.-W. Oh, D.-J. Lee, M.-K. Park, K. H. Park, J.-H. Lee, B. K. Kim, H.-R. Kim, *J. Phys. D: Appl. Phys.* **2015**, *48*, 405502.
[3] H. W. Chen, J.-H. Lee, B.-Y. Lin, S. Chen, S.-T. Wu, *Light: Sci. Appl.* **2018**, *7*, 17168.
[4] Y. Liu, J. Lai, X. Li, Y. Xiang, J. Li, J. Zhou, *I EEE Photonics J.* **2017**, *9*, 6900207.
[5] J. C. Choi, J.-W. Lee, D.-J. Lee, Y. K. Park, H.-R. Kim, *Adv. Eng. Mater.* **2021**, *23*, 2100174.
[6] N. Akamatsu, W. Tashiro, K. Saito, J.-I. Mamiya, M. Kinoshita, T. Ikeda, J. Takeya, S. Fujikawa, A. Priimagi, A. Shishido, *Sci. Rep.* **2014**, *4*, 5377.
[7] H. M. J. Boots, J. G. Kloosterboer, C. Serbutoviez, F. J. Touwslager, *Macromolecules* **1996**, *29*, 7683.
[8] D. Coates, *J. Mater. Chem.* **1995**, *5*, 2063.
[9] M. H. Saeed, S. Zhang, Y. Cao, L. Zhou, J. Hu, I. Muhammad, J. Xiao, L. Zhang, H. Yang, *Molecules* **2020**, *25*, 5510.
[10] L. G. Chen, R. Shanks, *Liq. Cryst.* **2007**, *34*, 1349.
[11] S.-H. Yoo, M.-K. Park, J.-S. Park, H.-R. Kim, *J. Opt. Soc. Korea* **2014**, *18*, 753.
[12] N. H. Cho, P. Nayek, J. J. Lee, Y. J. Lim, J. H. Lee, S. H. Lee, H. S. Park, H. J. Lee, H. S. Kim, *Mater. Lett.* **2015**, *153*, 136.

[13] N. H. Park, S. C. Noh, P. Nayek, M.-H. Lee, M. S. Kim, L.-C. Chien, J. H. Lee, B. K. Kim, S. H. Lee, *Liq. Cryst.* **2015**, *42*, 530.
[14] S.-G. Kang, J.-H. Kim, *Opt. Express* **2013**, *21*, 15719.
[15] B. Kim, H. G. Kim, G.-Y. Shim, J.-S. Park, K.-I. Joo, D.-J. Lee, J.-H. Lee, J.-H. Baek, B. K. Kim, Y. Choi, H.-R. Kim, *Appl. Opt.* **2018**, *57*, 119.
[16] H. Kikuchi, M. Yokota, Y. Hisakado, H. Yang, T. Kajiyama, *Nat. Mater.* **2002**, *1*, 64.
[17] Y. Yang, L. Wang, H. Yang, Q. Li, *Small Sci.* **2021**, *1*, 2100007.
[18] L. Rao, Z. Ge, S.-T Wu, S. H. Lee, *Appl. Phys. Lett.* **2009**, *95*, 231101.
[19] E. Kemiklioglu, L.-C. Chien, *Liq. Cryst.* **2017**, *44*, 722.
[20] S. Pagidi, R. Manda, H. S. Shin, J. Lee, Y. J. Lim, M. Kim, S. H. Lee, *J. Mol. Liq.* **2021**, *322*, 114959.
[21] H. Choi, M. Tanaka, T. Hiragun, M. Hide, K. Sugimoto, *Nanomed.: Nanotechnol. Biol. Med.* **2014**, *10*, 313.
[22] T. Kawano, M. Sato, H. Yabu, M. Shimomura, *Biomater. Sci.* **2014**, *2*, 52.
[23] Y. Hirai, H. Yabu, Y. Matsuo, K. Ijiro, M. Shimomura, *J. Mater. Chem.* **2010**, *20*, 10804.
[24] F. Galeotti, W. Mróz, G. Scavia, C. Botta, *Org. Electron.* **2013**, *14*, 212.
[25] Y. Ma, C. Fang, B. Ding, G. Ji, J. Y. Lee, *Adv. Mater.* **2013**, *25*, 4646.
[26] N. Q. Zhang, J. Li, D. Ni, K. N. Sun, *Appl. Surf. Sci.* **2011**, *258*, 50.
[27] J. Liang, Y. Ma, S. Sims, L. Wu, *J. Mater. Chem. B* **2015**, *3*, 1281.
[28] P. Jiang, M. J. McFarland, *J. Am. Chem. Soc.* **2004**, *126*, 13778.
[29] P. Jiang, T. Prasad, M. J. McFarland, V. L. Colvin, *Appl. Phys. Lett.* **2006**, *89*, 011908.
[30] J. M. Bueno, E. Berrio, M. Ozolinsh, P. Artal, *J. Opt. Soc. Am. A* **2004**, *21*, 1316.
[31] A. Ambirajan, D. C. Look, *Opt. Eng.* **1995**, *34*, 1651.
[32] J. M. Bueno, *J. Opt. A: Pure Appl. Opt.* **2000**, *2*, 216.
[33] J. H. Zhang, P. Zhan, Z. L. Wang, W. Y. Zhang, N. B. Ming, *J. Mater. Res.* **2003**, *18*, 649.
[34] H. Yang, P. Jiang, *Langmuir* **2010**, *26*, 12598.
[35] H. Yang, P. Jiang, *Langmuir* **2010**, *26*, 13173.
[36] A. I. Y. Tok, F. Y. C. Boey, Y. C. Lam, *Mater. Sci. Eng.* **2000**, *280*, 282.
[37] X. Feng, M. A. Meitl, A. M. Bowen, Y. Huang, R. G. Nuzzo, J. A. Rogers, *Langmuir* **2007**, *23*, 12555.
[38] L. B. Rothman, *J. Electrochem. Soc.* **1980**, *127*, 2216.
[39] M. Jiao, J. Yan, S.-T. Wu, *Phys. Rev. E* **2011**, *83*, 041706.
[40] J. Yan, L. Rao, M. Jiao, Y. Li, H. C. Cheng, S. T. Wu, *J. Mater. Chem.* **2011**, *21*, 7870.
[41] J. M. Bueno, M. Ozolinsh, G. Ikaunieks, *Ferroelectrics* **2008**, *370*, 18.
[42] S. K. Manna, L. Dupont, G. Li, *J. Phys. Chem. C* **2016**, *120*, 17722.
[43] T. Setälä, A. Shevchenko, M. Kaivola, A. T. Friberg, *Phys. Rev. E* **2002**, *66*, 016616.
[44] H. J. Kim, M. J. M. Krane, K. P. Trumble, K. J. Bowman, *J. Am. Ceram. Soc.* **2006**, *89*, 2769.
[45] Y. T. Chou, Y. T. Ko, M. F. Yan, *J. Am. Ceram. Soc.* **1987**, *70*, C-280.
[46] Y. J. Lim, J. H. Yoon, H. Yoo, S. M. Song, R. Manda, S. Pagidi, M.-H. Lee, J.-M. Myoung, S. H. Lee, *Opt. Mater. Express* **2018**, *8*, 3698.
[47] J. H. Yu, H.-S. Chen, P.-J. Chen, K. H. Song, S. C. Noh, J. M. Lee, H. Ren, Y.-H. Lin, S. H. Lee, *Opt. Express* **2015**, *23*, 17337.
[48] C.-H. Chang, Y.-H. Lin, V. Reshetnyak, C. H. Park, R. Manda, S. H. Lee, *Opt. Express* **2017**, *25*, 19807.
[49] H. hakemi, *Mol. Cryst. Liq. Cryst.* **2019**, *681*, 12.
[50] K. Li, H. Jiang, M. Cheng, Y. Li, Z. Yin, D. Luo, X. W. Sun, Y. J. Liu, *Liq. Cryst.* **2020**, *47*, 238.
[51] N. S. Oh, Y.-H. Shin, H.-Y. Kang, S.-B. Kwon, *Mol. Cryst. Liq. Cryst.* **2017**, *644*, 137.
[52] H. Mori, Y. Itoh, Y. Nishiura, T. Nakamura, Y. Shinagawa, *Jpn. J. Appl. Phys.* **1997**, *36*, 143.
[53] S. H. Hwang, Y. J. Lim, M.-H. Lee, S. H. Lee, G.-D. Lee, H. Kang, K. J. Kim, H. C. Choi, *Curr. Appl. Phys.* **2007**, *7*, 690.
[54] D. W. Kwon, Y. J. Lim, E. J. Jeon, D. H. Kim, J.-H. Kim, P. Kumar, M.-H. Lee, S. H. Lee, *Curr. Appl. Phys.* **2011**, *11*, 725.
[55] M. Oh-E, M. Yoneya, M. Ohta, K. Kondo, *Liq. Cryst.* **1997**, *22*, 391.
[56] D.-J. Lee, S.-W. Oh, G.-Y. Shim, J.-C. Choi, J.-H. Lee, B. K. Kim, H.-R. Kim, *J. Opt. Soc. Korea* **2016**, *20*, 156.
[57] S.-W. Oh, D.-J. Lee, M.-K. Park, K. H. Park, J.-H. Lee, B. K. Kim, H.-R. Kim, *J. Phys. D: Appl. Phys.* **2015**, *48*, 13.
[58] T. R. Lee, J. H. Kim, S. H. Lee, M. C. Jun, H. K. Baik, *Liq. Cryst.* **2017**, *44*, 1146.
[59] K. V. Le, S. Aya, Y. Sasaki, H. Choi, F. Araoka, K. Ema, J. Mieczkowski, A. Jakli, K. Ishikawa, H. Takezoe, *J. Mater. Chem.* **2011**, *21*, 2855.
[60] S. Pagidi, R. Manda, S. S. Bhattacharyya, K. J. Cho, *Composites, Part B* **2019**, *164*, 675.
[61] D. Franklin, Y. Chen, A. Vazquez-Guardado, S. Modak, J. Boroumand, D. Xu, S.-T. Wu, D. Chanda, *Nat. Commun.* **2015**, *6*, 7337.